 doi:10.20944/preprints202207.0169.v1

Article

Influence of Powder Characteristics on the Microstructure and Mechanical Behaviour of GH4099 Superalloy Fabricated by Electron Beam Melting

Shixing Wang[1], Shen Tao[2] and Hui Peng[2,3,*]

[1] School of Materials Science and Engineering, Beihang University, 37 Xueyuan Road, 100191 Beijing, China; wsx161@163.com
[2] Research Institute for Frontier Science, Beihang University, 37 Xueyuan Road, 100191 Beijing, China; taoshen@buaa.edu.cn
[3] Key Laboratory of High-Temperature Structural Materials & Coatings Technology, Ministry of Industry and Information Technology, Beihang University, 37 Xueyuan Road, 100191 Beijing, China; penghui@buaa.edu.cn
[4] Surface Engineering Research Institute, Chinese Academy of Agricultural Mechanization Sciences, No. 1 Beishatan Road, 100191 Beijing, China; +86-13811027105
*Correspondence: penghui@buaa.edu.cn; Tel.: +86-(010)-82317117

Abstract: A Chinese superalloy GH4099 (~20 vol.% γ′ phase), which can operate for long periods of time at temperatures of 1173-1273 K, was fabricated by electron beam melting (EBM). Argon gas atomized (AA) and plasma rotation electrode process (PREP) powders with the similar composition and size distribution were used as raw materials for comparison. Microstructure and mechanical properties of both the as-EBMed and post-treated alloy samples were investigated. The results show that the different powder characteristics resulted in the different build temperatures for AA and PREP samples, which were 1253 K and 1373 K, respectively. With increasing the building temperature, the EBM processing window shifted towards the higher scanning speed direction. Furthermore, intergranular cracking was observed for the as-fabricated PREP sample as a result of local enrichment of Si at grain boundaries. The cracks were completely eliminated by hot isostatic pressing (HIPing) and did not re-open during subsequent solution treatment and aging (STA). Fine spherical γ′ phase precipitated uniformly after STA. The tensile strength of the HIP+STA samples was ~920 MPa in the building direction and ~850 MPa in the horizontal direction, comparable with that of the wrought alloy.

Keywords: Ni-based superalloys; electron beam melting; additive manufacturing; Argon gas atomized; plasma rotation electrode process; powder characteristics

1. Introduction

Ni-based superalloys are widely used in hot sections in aerospace industry for their excellent high temperature mechanical properties and oxidation/corrosion resistance [1]. Recently, powder-bed based additive manufacturing (AM), including both selective laser melting (SLM) and electron beam melting (EBM), are utilized for fabricating complex superalloy parts [2, 3]. Several previous works demonstrated the feasibility of fabricating dense and crack free superalloys with tailored microstructure [4-9]. Ultra-fine crystallographic grain structure was commonly observed in the SLMed superalloys, owing to the rapid solidification rate and high temperature gradients within the micro melt pool. By contrast, coarser columnar grains were usually formed in the EBMed superalloys under preheated conditions [2, 10]. Particularly, by careful controlling the process parameters, a columnar to equiaxed (CET) transition of grains was realised [11-14]. Besides, it has also been demonstrated that the mechanical properties of some AM superalloys are comparable to that of the wrought and cast superalloys [15, 16].

Preprints (www.preprints.org) | NOT PEER-REVIEWED | Posted: 12 July 2022 doi:10.20944/preprints202207.0169.v1

According to the content of Al and Ti, superalloys can be divided into two categories, weldable or non-weldable (Figure 1) [17]. The level of Al + Ti determines the volume fraction of γ′ precipitates within the superalloy, which plays an important role in the high-temperature strength and creep resistance [16, 18, 19]. Unfortunately, superalloys with high amount of γ′ precipitates are considered to be difficult to weld because of their high tendency to crack, particularly the phenomenon of hot cracking [4, 20]. Current SLM and EBM are developed based on welding technologies, it is therefore that processing of non-weldable superalloys brings challenges to AM.

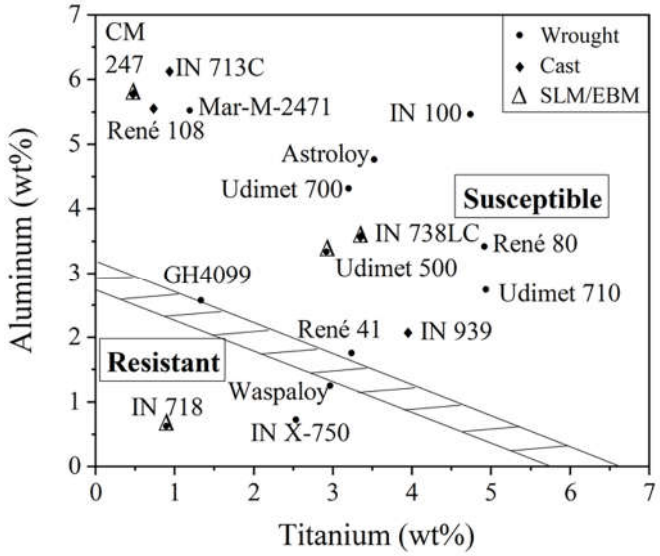

Figure 1. Effect of Ti and Al content on susceptibility of Ni-base superalloys to cracking associated with welding process. The diagram was adapted from [17] and the latest work from SLM/EBM have been included as well as GH4099.

Some recent published works are focusing on the cracking mechanisms of AM non-weldable superalloys. It has been revealed in Ref. [20] that the hot cracking behaviour is attributed to the presence of a liquid film during the last stage of solidification and thermal stresses. A correlation between cracks and high angle grain boundaries (HAGB) was identified. It is also confirmed by atom probe tomography (APT) that a local enrichment of minor element B at the grain boundaries is responsible for the formation of a liquid film at HAGB [20]. Further works performed by Körner [16] and Martin [8] demonstrate the feasibility of producing single crystal superalloy by EBM, in which crack free samples of a nonweldable Ni-based superalloy were successfully obtained by eliminating grain boundaries via competitive grain growth. A very recent work proposed the atomic-grain boundary design [4]. Although these innovative results have aroused widespread interest in additive manufacturing of superalloys, hot cracks yielded in polycrystalline non weldable superalloys (columnar or equiaxed grain structure) remain unresolved.

Decreasing the level of γ′ precipitates in the nonweldable superalloy can reduce the cracking tendency significantly. However, a proper amount of γ′ precipitates is desirable for adequate mechanical strength. For certain high-temperature applications, the amount of γ′ precipitates should be optimized to achieve the best balance of strength and weldability. An example of this is the relatively newly designed γ′-strengthened superalloy, HAYNES 282, which was developed for applications in both aero and land-based gas turbine engines [21]. The total γ′ forming elements (Al + Ti) content of HAYNES 282 is 3.7 wt.%, with the γ′ mole fraction of ~19 %. The carefully selected γ′ precipitates level ensures the alloy has a combination of satisfied mechanical properties and improved weldability, compared with the typical non weldable superalloy.

In this work, a Chinese superalloy GH4099 was fabricated by electron beam melting. This alloy has a similar γ′ precipitates level with HAYNES 282, and can operate for long term at temperatures of 1173-1273 K. The objective of following investigation is to exhibit

Preprints (www.preprints.org) | NOT PEER-REVIEWED | Posted: 12 July 2022 doi:10.20944/preprints202207.0169.v1

the influence of raw powder characteristics on the microstructure of the EBMed superalloy. The mechanism of minor element Si on the cracking behaviour was elucidated. Cracks evolution during heat treatment and mechanical properties of the samples were also concerned.

2. Experimental

2.1. GH4099 Powders

Argon gas atomized (GA) and plasma rotating electrode process (PREP) GH4099 powders were used as raw material, which were provided by CASIC-HUNAN and CISRI-GAONA, China, respectively. Table 1 shows the chemical composition of both GA and PREP powders was measured by inductively coupled plasma atomic emission spectroscopy (ICP-OES). The chemical composition of the raw powders was compared with the nominal composition, as shown in Table 2. It can be seen that the two powders were provided with similar composition, except for that the Si content in the PREP powders is almost one order of magnitude higher than that of the GA powders. Note that the 0.285 wt.% of Si is quite close to maximum limit of the nominal composition. A comparison of the powder morphology is shown in Figure 2. Satellites and micro particles can be observed for the GA powders, as compared with the perfect spherical PREP powders. Figure 3 exhibits similar size distribution curves for the two powders measured by a laser granulometry (Bettersize, 9300ST) within the size range between 45 μm and 140 μm, both with an average size of ~90 μm. Powder properties include specific surface area (SSA, m^2/kg), flowability, bulk density, packing density and D90 etc. were shown in Table 3, The tap density of powders was determined to be 4.53 g/cm^3 and 4.89 g/cm^3. Flow time of 16.4 s and 15.4 s were measured by a Hall flowmeter with 2mm hole.

Table 1. Chemical composition of GA and PREP powders of GH4099 (wt.%).

Powder Type	Element content, wt.%							
Argon gas atomised (GA)	Cr	Co	W	Mo	Ti	Al	Fe	Mn
	18.21	6.44	5.88	4.00	1.29	2.03	<0.1	<0.005
	Si	C	N	O	Ni			
	0.025	<0.1	0.005	0.008	Bal.			
Plasma rotating electrode process (PREP)	Cr	Co	W	Mo	Ti	Al	Fe	Mn
	18.65	5.91	5.91	3.89	1.29	2.26	0.54	0.24
	Si	C	N	O	Ni			
	0.285	<0.1	0.003	0.008	Bal.			

Table 2. Nominal composition of GH4099 (wt.%).

Element	**Ni**	**Mo**	**Fe**	**Cr**	**W**	**Al**	**Ti**
Content	Bal.	3.50-5.00	≤3.00	17.50-19.50	5.50-7.00	2.50-3.00	1.00-1.50
Element	**Co**	**Si**	**B**	**Mn**	**Cu**	**Ce**	**S/P**
Content	5.00-8.00	≤0.30	≤0.005	≤0.30	≤0.070	≤0.020	≤0.015

Preprints (www.preprints.org) | NOT PEER-REVIEWED | Posted: 12 July 2022 doi:10.20944/preprints202207.0169.v1

Table 3. Powder properties of two types of GH4099.

Powder	SSA (m^{-2}/kg)	Flowability (s)	Packing density (g/cm^3)	D10 (μm)	D50 (μm)	D90 (μm)
GA	32.91	16.4	4.53	49.68	92.57	155.0
PREP	28.36	15.4	4.89	52.74	84.00	133.8

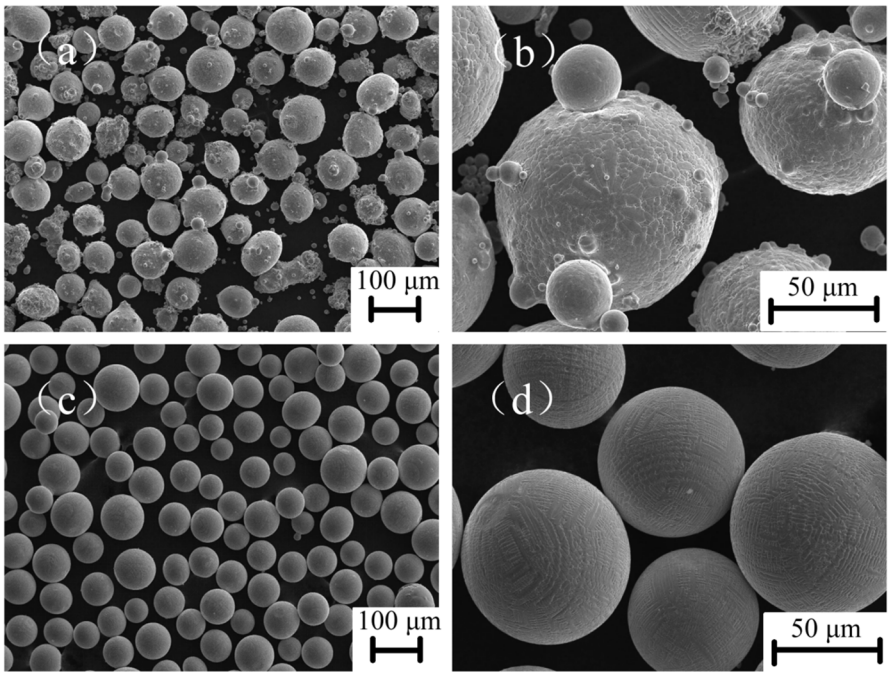

Figure 2. SEM morphology of pre-alloyed GH4099: (**a,b**) GA; (**c,d**) PREP.

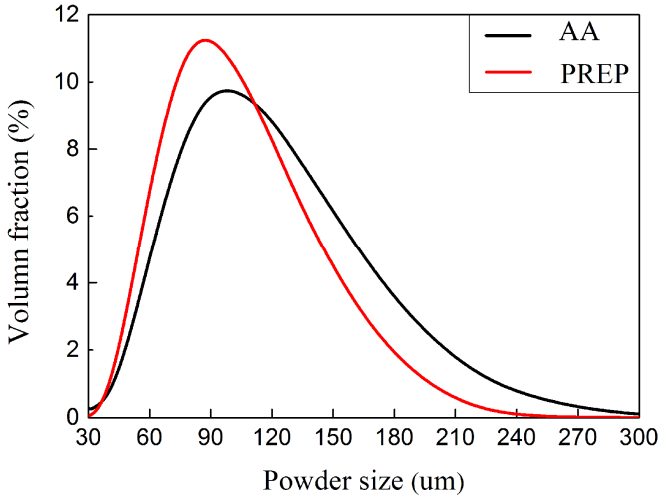

Figure 3. Volume fraction distribution of powder particles.

2.2. EBM Sample Fabrication

GH99 superalloy samples were fabricated using Arcam A2XX machine with Control Software 3.2 in a manual mode. Figure 4a shows the schematic diagram of one batch of as-EBM samples. Layers were scanned using a snake-like melting strategy (i.e. either 0° or 90° hatch direction is used for each layer), showing in Figure 4b. 10 mm thick stainless steel plate with a diameter of 150 mm was used as starting plate. No supports were applied for the EBM fabrication. One batch of the EBM fabrication included 9 with each 20 value × 20 value × 30 value mm in X-Y-Z dimension. EBM process windows were firstly established for the GA powders by using a range of scanning speed *v* from 333-9000 mm/s,

Preprints (www.preprints.org) | NOT PEER-REVIEWED | Posted: 12 July 2022 doi:10.20944/preprints202207.0169.v1

combined with a range of line offset L_{off} from 0.1-0.3 mm, followed by PREP powders. Three different beam current I values of 5 mA, 10 mA, and 15 mA were selected. This resulted in equivalent area energy EA values ranging from 0.414 J/mm² to 3 J/mm². An EBM operating voltage of 60 kV was used. The area energy calculation was based on the classic formula that are commonly used for EBM, as reported in our previous work. According to the results of powder sintered tests, 980 ℃ and 1100 ℃ with optimum effects of sintering were selected as the final forming temperature of GA powder and PREP powder, respectively.

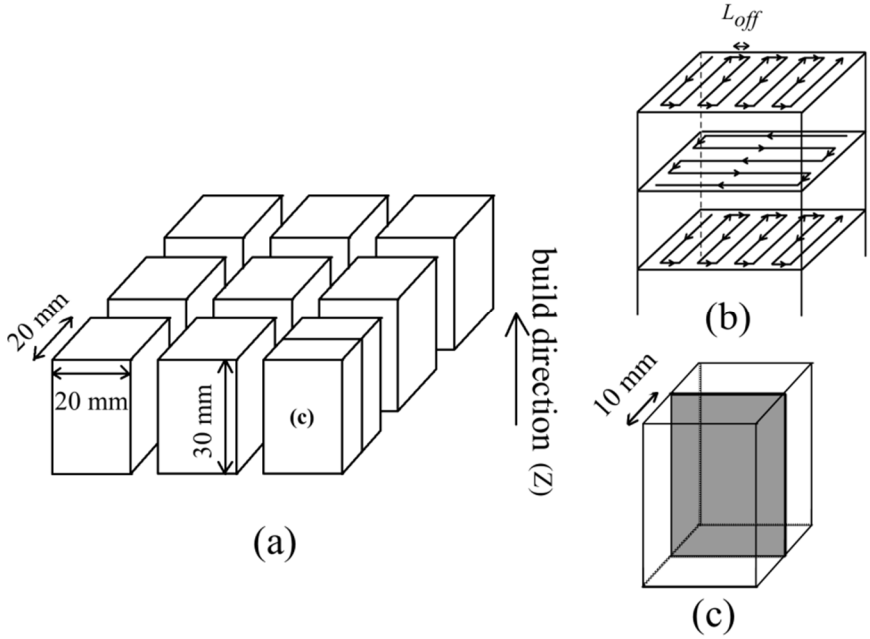

Figure 4. Schematic diagrams of (**a**) one batch of as-EBM samples; (**b**) electron beam scans in a cross snake-like way with a specific L_{off} and hatching layer of 50 μm; (**c**) shows the microstructural characterization region demonstrated in Fig. 4(a).

2.3. Microstructural Characterisation

The samples were investigated by optical microscopy (Leica DM 4000) and cut parallel to the build direction (Z-direction) from the centre location of the as-EBM samples (depicted in Figure 4c). Standard metallographic procedures including grinding and polishing were performed for microstructure characterization. A Zeiss Gemini SEM 300 scanning electron microscopy was used for microstructural observation. The metallographic etching selected for observing grain morphology was 4g $CuSO_4$, 100 mL HCl and 100 mL H_2O for 1 min. The polished specimens were electro-etched for 6 s at 5 V in a solution of 12 mL H_3PO_4, 40 mL HNO_3 and 48 mL H_2SO_4 to reveal γ′ precipitates morphology. Cracks were evaluated based on the investigation of both the fracture sections and polished sections in Z direction by employing optical microscope and SEM of secondary electron imaging. Samples with poor conductivity were subjected to spray-gold treatment to improve conductivity. An electro-probe microanalyzer (EPMA, JEOL JXA-8100) was also employed to detect the minor elements distribution at the vicinity of grain boundaries. One thing should be mentioned is that in order to prevent elements contamination during sample preparation, the EPMA samples were cut by diamond wire, ground by diamond abrasive papers and polished by diamond slurry.

2.4. Post-processing

The samples with internal cracks were healed by hot isostatic pressing (HIP) at 1150 ℃, 150 MPa for 4 h, followed by furnace cooling to room temperature, which referred to as EBM+HIP. In order to eliminate butterfly-like γ′ phases and improve its mechanical

Preprints (www.preprints.org) | NOT PEER-REVIEWED | Posted: 12 July 2022 doi:10.20944/preprints202207.0169.v1

properties, selected EBM+HIP samples were then exposed to a standard solution and aging treatment (STA) process (i.e. solution treated with a temperature of 1200 ℃ for 1h, followed by quenching oil cooling to room temperature, then giving an aging treatment of 900 ℃ for 4 h, followed by quenching oil cooling to room temperature) referred to as EBM+HIP+STA. It is worthy of noting that the purpose of solution treatment is to make unevenly distributed γ′ precipitations further re-dissolved into the γ matrix, i.e. the uniform precipitation of γ′ phases, and to readjust the morphology of γ′ phase by changing aging temperature, aging time or cooling method, so as to realize precipitation strengthening and improve the mechanical properties of the Ni-based superalloy.

2.5. Mechanical Property Characterization

Micro-hardness measurements by FM-800 microhardness tester from FUTURE-TECH (Japan) were performed on as-EBM, as-EBM+HIP and as-EBM+HIP+STA conditions as well as the cast GH4099 samples with the load of 200 g and holding time of 10 s. To ensure measurement data validation and accuracy, 10 measurements points per sample from top to the bottom divided into four regions were performed and average values together with error are obtained here. The indentation should be on the straight line as far as possible.

Tensile tests were performed on these specimens at room temperature using an electronic universal testing machine (MTS Industrial Systems (China) Co. SANS CMT4000). Micro deformation was measured by electronic extensometer. Specific methods were as follows:

(1) The first stage: extensometer of strain to be 0.0001mm/s, desired force to be 1300N.
(2) The second stage: extensometer of strain to be 0.000025mm/s, desired force to be 1800N.
(3) The third stage: extensometer of strain to be 0.000025mm/s, desired force to be 5000N.

3. Results

3.1. Characteristics of Starting Powders for EBM Process

Gas Atomization is completed by the molten metal which is atomized due to inert gas jets into fine metal droplets, then cool down in the atomizing tower. Plasma-rotating Electrode Process is a centrifugal atomization process in vacuum atmosphere developed by Starmet in which plasma arc is involved, and this method is currently a leading candidate for high-purity powders of metals with high melting point such as Ti and Ni alloys powders production [22-24].

Representative micrographs (SEM) of atomized powders are shown in Figure 2a,b for GA powders and Figure 2c,d for PREP powders. In general, PREP powders shown in Figure 2c exhibited a much better spherical shape compared to GA powders, Figure 2a. In addition, little satellite particles can be found in PREP powders, Figure 2c,d. As described in [25], powder particle size distribution and its mean size have traditionally been considered to be important which have a certain impact on packing density on the build plate as well as the density of finished part. Powders with smaller average particles (D50) have been found to result in better surface roughness of the completed samples according to [26], Large particles might not be fully melt and fuse, conversely too-small particles can lead to ball, spatter or swell causing too much energy [27]. However, there are many particle properties that could potentially influence the overall behaviour of the powder for the subsequent EBM process. These key particle properties include specific surface area, flowability, packing density and D90.

Figure 5 shows the interior morphology of GH4099 powder particles. It's clearly that the interior of GA powder particles were massive cellular dendrites (Figure 5a,b), due to the rapid solidification during the cooling process. The interior morphology of PREPed GH4099 powder particles were mainly segregated dendritic and light of cellular dendrites (Figure 5c,d), resulted from different cooling rate between mental liquid and matrix in the solidification process [24], making these dendrites growing up and getting coarse.

Preprints (www.preprints.org) | NOT PEER-REVIEWED | Posted: 12 July 2022 doi:10.20944/preprints202207.0169.v1

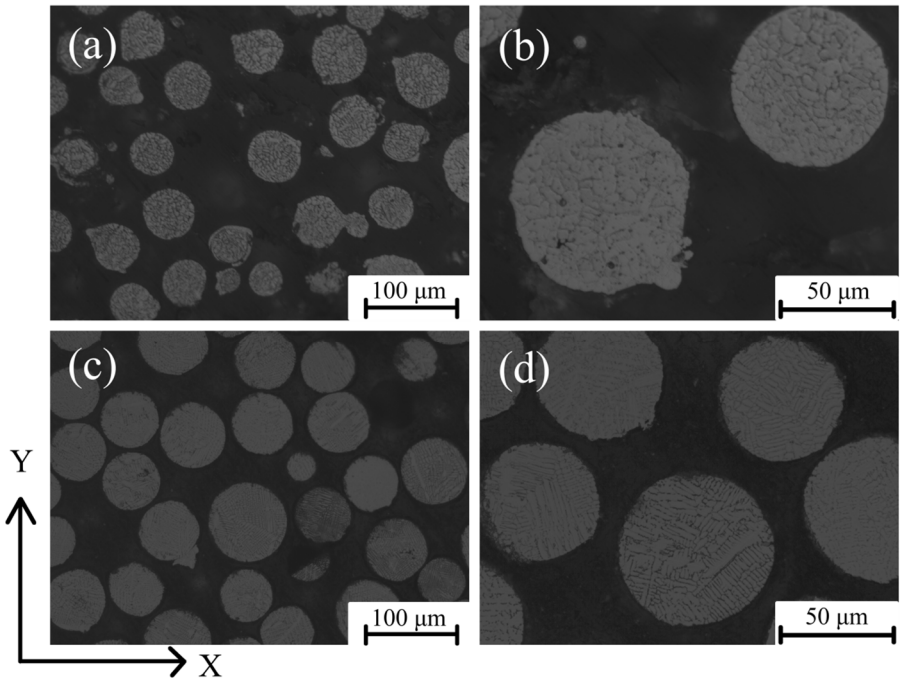

Figure 5. SEM micrographs of cross-section of interior crystalline structure in particles (**a,b**) GA; (**c,d**) PREP.

3.2. Process Window

According to the results of OM and SEM, these samples with two types of defects, namely, uneven and bonding defect in micromorphology, were made into the EBM process window based on the varying melting current and scanning speed as well as the dense samples with no surface unevenness, which had been divided into two forming windows according to the different powder used for the samples, as shown in Figure 6. With increasing the build temperature, the EBM processing window shifts towards the higher speed and lower energy exposure per area E_A (in J·m^{-2}) direction. Due to the different powder characteristics, the PREP powders are more difficult to be sintered during preheating of the powder bed by electron beam. This resulted in a higher build temperature for the PREP powders than the GA powders.

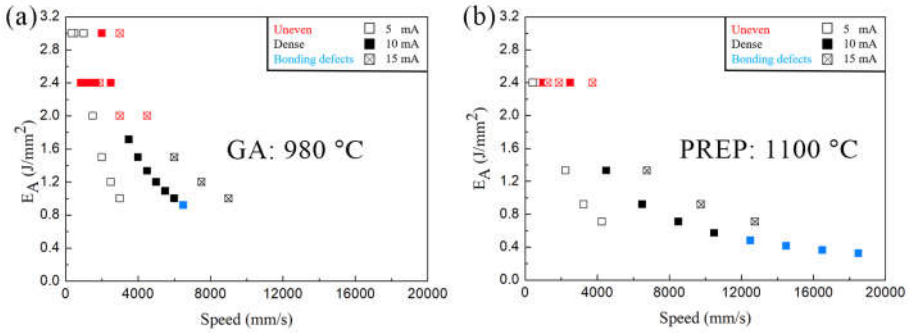

Figure 6. EBM processing window identified for GH99 superalloy: suitable conditions resulting in dense samples with no top surface unevenness are indicated by black symbols. Process parameters varied are line offset (L_{off}), beam melting current (I) and scanning speed (v). (**a**) GA powders and (**b**) PREP powders.

Binding defects occur with increasing scanning speed when the energy input is too low for complete melting of the powder layer leaving the longitudinal pores [7]. Unevenness on the surface occurs with lower deflection speeds and higher scanning current of the electron beam. Helmer et al. [28] reported that unevenness of the top surface is a result of vigorous melt pool motion caused by high forces exerted on the melt pool which could

Preprints (www.preprints.org) | NOT PEER-REVIEWED | Posted: 12 July 2022 doi:10.20944/preprints202207.0169.v1

be interpreted as temperature gradients, surface energy effects (Marangoni convection) and evaporation.

3.3. Microstructural Characterization

Columnar crystals and the equiaxial crystals were observed in as-EBM condition samples deposited with GA powder and PREP powder, Besides, an obvious columnar to equiaxed transition (CET) was also observed for both powders within the processing window, which is not shown here.

Two samples made from GA and PREP powders were selected for detailed investigations. As can be seen in Figure 7a,b, both samples reveal a similar columnar grain width of ~200 μm. The average grain width of the EBM sample deposited with GA powder (GA sample) as well as the sample as-EBM condition deposited with PREP powder (PREP sample) are 195.16±18.46 μm and 206.47±28.74 μm, respectively. SEM images of the γ′ precipitations are shown in Figure 7c,d. The distribution of the γ′ is quite homogeneous in the as-EBM state, with a volume fraction of about 20 % for both samples. The γ′ is seen to be spherical and very fine in size. Different from the limited formation of γ′ in the as-SLMed superalloys [29], the processing conditions (rapid solidification and high build temperature) of EBM fabrication may provide a proper thermal history for the precipitation of γ′. It is therefore not surprising that the higher build temperature resulted in a larger γ′ precipitated (~90 nm) in the PREP sample than that of the GA sample (~130 nm).

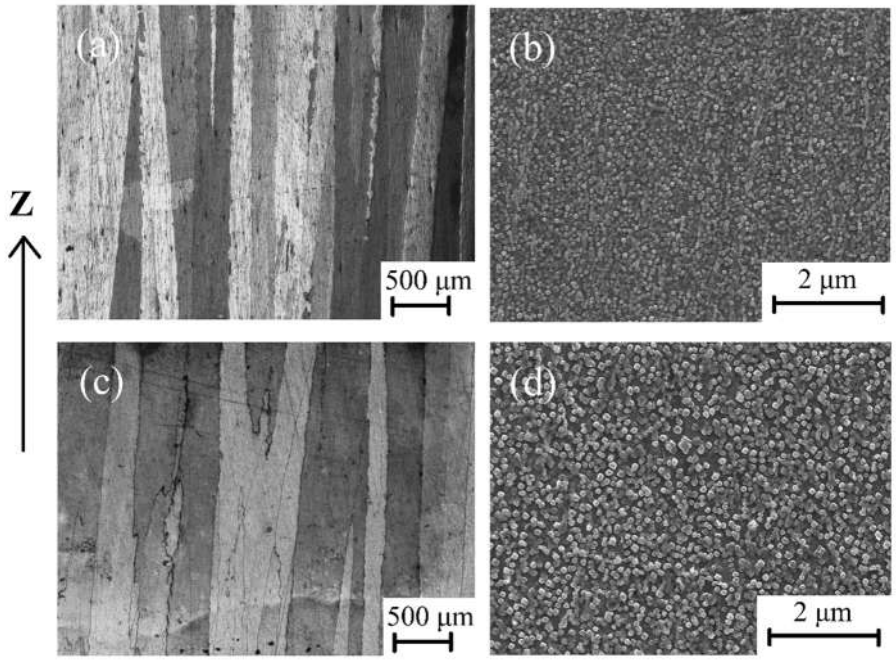

Figure 7. Optical micrographs in the X-Z plane of GH4099 samples fabricated by EBM deposited with: (**a**) GA; (**c**) PREP powder, and SEM micrographs of γ′ phase as-EBM GH4099 samples showing the morphology of γ′ precipitates: (**b**) GA; (**d**)PREP.

3.4. Cracking in as-EBM GH4099 Superalloy

Macro cracks were not observed on the external surface and the wire-cut surface of the as-EBM GH4099 samples. However, the micro-cracks existed in the samples deposited with PREP powder by optical microscope and scanning electron microscope after grinding and polishing, conversely, not in the samples deposited with GA powder. The cracks are parallel to the building direction, and no transverse cracks or lack of fusion appear, Figure 8. These microcracks are distributed along the columnar grain boundaries, which indicates that the microcracks are intergranular cracks.

Preprints (www.preprints.org) | NOT PEER-REVIEWED | Posted: 12 July 2022 doi:10.20944/preprints202207.0169.v1

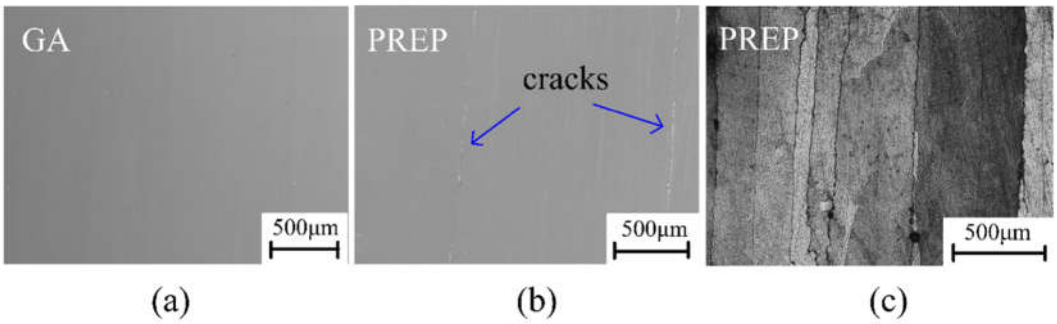

Figure 8. Cracks morphology of as-EBM GH4099: optical micrographs of un-etched (**a**) GA sample with no cracks and (**b**) PREP sample with cracks parallel to the building direction. (**c**) etched PREP sample showing the microcracks are intergranular cracks.

Observation of the polished cross-section are shown in Figure 8a,b. It can be seen that the GA sample is dense and crack-free. However, micro-cracks were detected in the PREP sample, with the cracking ratio determined to be ~5% in area fraction. The occurrence of cracks is associated with formation of liquid films at grain boundaries, as indicated by arrows shown in Figure 8b. Figure 8c also confirms that the microcracks are intergranular cracks.

3.5. Crack Healing and Microstructural Evolution

Kirka et al. [30] found that holes in Inconel 718 Alloy formed by EBM could be removed by hot isostatic pressing. Carter [31] et al. found that cracks in CM247LC alloy formed by SLM could be eliminated by hot isostatic pressing. Therefore, in order to eliminate the micro-cracks in as-EBM sample, selected PREP sample was given a HIP treatment. The SEM micrograph of the GH4099 after HIPing indicate that HIP can eliminate the micro-cracks in as-EBMed GH4099, Figure 9a,b shows the microstructure evolution of γ′ phase and the coarse irregular-shaped γ′ phase after HIPing appeared with the HIP temperature close to the initial melting point of GH4099 between 1150 ℃ and 1180 ℃, which may affect the microstructure of the sample. Due to the hatching temperature of 1150 ℃ is much higher than 950 ℃ in the process window, while the hatching time of a batch of samples is about 30 h, achieved part retained its heat for a long time, which was equivalent to a high temperature solution treatment of the sample, after a long period of heat preservation, γ′ phases were sufficiently precipitated and grown up.

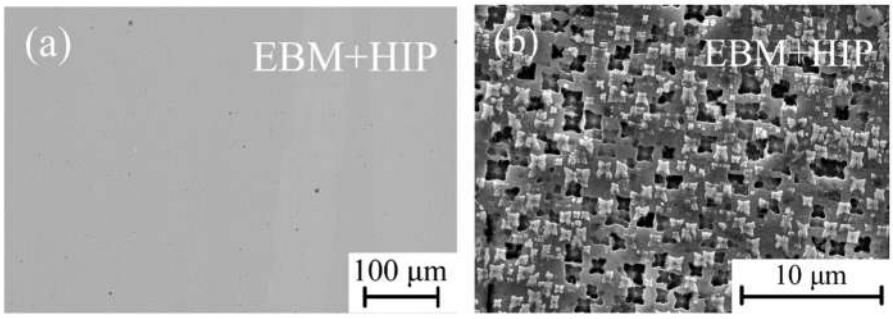

Figure 9. SEM micrographs of EBM+HIP GH4099 sample shows the crack healing after HIP and microstructural evolution in terms of γ′ precipitates.

Through various numerical simulations, Cha et al. [32] found that the growth rate in the <110> direction is enhanced due to a high chemical driving force while the migration rate in the <100> direction is suppressed due to enriched solute and a corresponding low chemical driving force. Then the growing shape transforms to a concave shape. The splitting occurs only in the concave growth condition and that it is induced by the interface instability, which is in good agreement with the experimental observations. Yoo et al. [33] found that morphological unstable and irregular growth in Ni base superalloy occurs

Preprints (www.preprints.org) | NOT PEER-REVIEWED | Posted: 12 July 2022 doi:10.20944/preprints202207.0169.v1

whenever there is enough supersaturation in the matrix so that the point effect of diffusion is operative with the change of morphology.

The resultant post-processed combined HIP with STA treatment EBM GH4099 microstructure is illustrated in Figure 10. Heat treatment has a pronounced effect on the structural related to microfissuring through the effect on solute solubility, grain size and/or the dissolution of phases [34]. Cracks were successfully closed and did not reopen after heat treatment, Figure 10a, which is different from our previous report of a non-weldable superalloy [6]. Figure 10b shows the features of γ′ precipitates for heat-treated samples. The coarse irregular-shaped γ′ was optimized into fine spherical particles and distribute more homogeneously on comparison with the HIPed sample after heat treatment, which plays an effective role in adjusting the microstructure of the GH4099 alloy. The HIP+STA treatment resulted in grain refinement, while γ′ precipitates with more volume fraction was found after the STA treatment when compared to that of the as-EBM material.

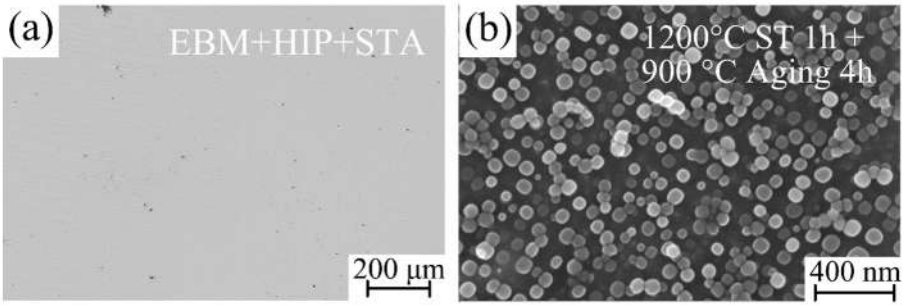

Figure 10. The cracking incident after HIP+STA and microstructural evolution in terms of γ′ precipitates. The internal structure appears to be crack-free in EBM+HIP+STA condition.

Table 4 summarizes the grain width and γ′ precipitates volume fraction of GH4099 superalloy in different conditions. The results show that the difference of γ′ volume fraction between GA and PREP powder deposited GH4099 alloys with similar columnar crystal grain widths is small. Passed through HIP treatment of the PREPed sample, the grain width reduced to 70.74±7.70 μm. Because the HIP temperature is 1150 ℃, which is close to the incipient melting temperature of the GH4099 alloy between 1150 ℃ and 1180 ℃, thus affecting the microstructure of the sample. For 4 hours heat preservation time during HIP process is far less than the 30 hours required for EBM forming a batch of samples, and the grains had insufficient time to grow. Undergoing STA treatment, the average grain width in the EBM+HIP condition of PREPed sample did not change significantly, but the number of γ′ precipitates increased. These results show that PREPed sample undergoing HIP treatment then exposed to 1200 ℃ for 1 hour + 900 ℃ for 4 hours STA treatment can not only completely eliminate the coarse irregular-shaped γ′ precipitates, but also improve the mechanical properties of the alloy without affecting the grain structure of the superalloy.

Preprints (www.preprints.org) | NOT PEER-REVIEWED | Posted: 12 July 2022 doi:10.20944/preprints202207.0169.v1

Table 4. Measured average grain width and γ′ volume fraction of as-EBM GAed and PREPed GH4099 samples and their changes due to HIP and STA treatment. The building parameters of the GAed and PREPed sample are listed here.

Sample	*I* (mA)	*v* (mm/s)	L_{off} (mm)	Grain width (μm)	γ′ volume fraction (%)
GA-EBM	5	3000	0.1	195.16±18.46	17.14±0.92
PREP-EBM	10	1250	0.2	206.47±28.74	16.10±0.48
PREP-EBM+HIP	-	-	-	70.74±7.70	-
PREP-EBM+HIP+STA	-	-	-	69.37±6.32	19.30±1.06

3.6. Mechanical Properties

The microhardness in the X-Z plane of GAed and PREPed samples under different conditions are compared with wrought GH4099 sample. The results show that the hardness value of the as-EBM GAed sample ~368 μm is equivalent to the wrought sample ~369μm, and is slightly lower than the hardness standard of the wrought GH4099 superalloy going through standard STA treatment ~376 μm. The mechanical properties of GH4099 nickel-based superalloy in EBM condition have basically reached the forging standard. The microhardness of PREPed GH4099 sample ~359 μm is slightly lower than that of wrought condition. As mentioned earlier, microcracks existed in the as-EBM PREPed specimens, and the hardness reflects the ability of the material to resist external force deformation. When measuring the microhardness at the same height of the prepared sample in a random manner, it is likely that the position of the measuring point is on or near the cracks, resulting in a decrease in the average value of the microhardness. At the same time, the standard deviation in microhardness measurement of the PREPed sample is also large, which may be due to inhomogeneous measuring points caused by the microcracks. The same case to GA sample is presumed as follows: GA powders were rapidly cooling and solidification by argon gas during the preparation process, and there were more or less porosities inside. Therefore, the gas therein cannot escape in such a short time during rapid solidification process, or the electron beam energy input is excessive into evaporation and ejection of the feedstock powders or molten materials, thereby generating pores in the deposited metals. Similarly, the unevenness measuring points nearby porosities lead to relatively big errors.

The microhardness in the X-Z plane of PREPed samples in EBM+HIP condition and EBM+HIP+STA condition was measured, compared with wrought GH4099 sample after a standard STA treatment. As shown in Figure 11, the microhardness of as-build PREPed sample decreases after the HIP treatment which is attributed to the closure of defects such as microcracks by the applied HIP treatment [35], with the γ′ phase of PREPed sample grew by unstable manner, resulting in a large amount of bigger irregular-shaped γ′ phase. The enhancement in mechanical properties of GH4099 nickel base superalloy is mainly due to precipitation strengthening effect with the main precipitates of γ′. It is beneficial to improve the mechanical properties as fine γ′ precipitates dispersing uniformly in the γ matrix. The strengthening effect of coarse irregular-shaped γ′ phase relative to the γ matrix will be greatly weakened, leading to the decrease of microhardness. Subsequent STA treatment of 1200 ℃ solid-solution for 1 hour + 900 ℃ aging for 4 hours caused γ′ phase to re-dissolve into the γ matrix in a fine dispersion during aging treatment.

Preprints (www.preprints.org) | NOT PEER-REVIEWED | Posted: 12 July 2022 doi:10.20944/preprints202207.0169.v1

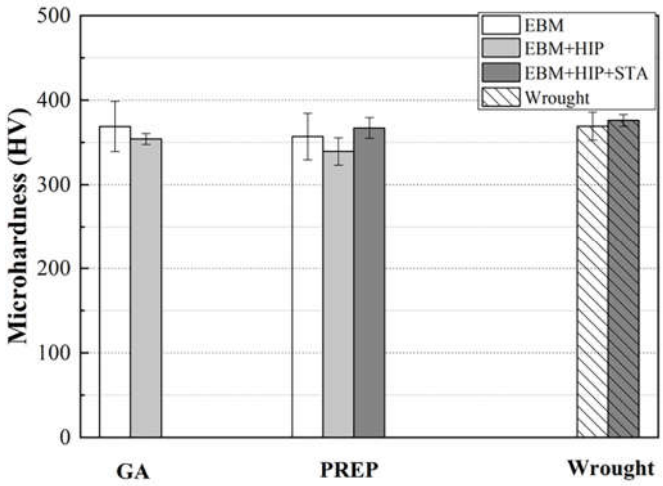

Figure 11. Measured average microhardness of GAed and PREPed GH4099 samples in EBM and EBM+HIP or EBM+HIP+STA condition compared with the wrought GH4099 in both as-wrought and wrought + STA conditions.

The elastic modulus and stacking fault energy between the two phases are different, which results in conformal strain and reinforcement effect on the alloy. Moreover, because of the larger specific area of the fine particles in the gamma phase, the reinforcement effect is significantly enhanced, which makes the PREP-EBM+HIP+STA specimens microscopic. Hardness has been improved. At the same time, cracks will not occur again after solution aging treatment, so its microhardness is higher than that of EBM state and EBM+HIP state. In the meanwhile, the cracks did not re-generate inside the sample after STA treatment, so its microhardness is notably enhanced compared with its in EBM and EBM+HIP conditions.

As-EBM GAed sample was subjected to the same standard STA treatment, strip tensile test specimen was cut parallel to the EBM building direction, its tensile strength at room temperature was measured, as well as in EBM+HIP+STA condition of PREPed samples which were cut parallel and perpendicular to the building direction, respectively. Above mentioned samples were compared with the tensile strength of wrought GH4099 sample and by the standard STA treatment at room temperature, as shown in the Figure 12.

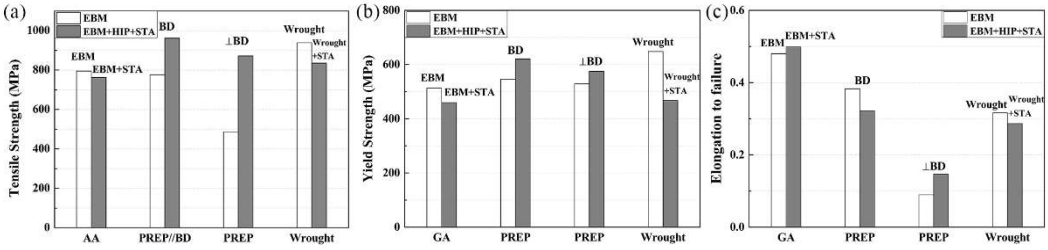

Figure 12. (**a**) Tensile strength, (**b**) yield strength and (**c**) elongation to failure of GAed and PREPed GH4099 sample in different conditions cut parallel or/and perpendicular to building direction, meanwhile compared with that of wrought sample along building direction.

Both of the tensile strength of as-EBM GH4099 samples are lower than that of wrought sample. Further, the tensile strength of the GAed sample is slightly higher than that of PREPed sample, which can be related to the small amount of pores inside GAed sample and microcracks existed in the PREPed sample. The tensile strength of post-processed PREPed sample along building direction was significantly improved than as-EBM sample due to elimination of microcracks after HIP treatment and re-dissolving and re-precipitating dispersed γ′ phase during STA treatment, which provide high mechanical strength about ~926 μm. Tensile strength of PREPed sample which was cut perpendicular

Preprints (www.preprints.org) | NOT PEER-REVIEWED | Posted: 12 July 2022 doi:10.20944/preprints202207.0169.v1

to the EBM building direction (i.e. perpendicular to the growth direction of the columnar crystal) about ~486 μm is significantly lower than that parallel to the building direction about ~775 μm, which can be related to intergranular cracks distributed in as-EBM PREPed sample along grain boundary, resulting in low intergranular bonding force. Cracks rapidly expanded while stretching along building direction then exhibited a low tensile strength. After HIP and STA treatments, tensile strength increased to ~757 μm and still slightly lower than as-EBM PREPed tensile specimen parallel to the building direction indicating the anisotropy in strength. Tensile strength of as-EBM GAed sample decreases undergoing STA treatment and the same for wrought GH4099 sample.

4. Discussion

4.1. Crack Mechanism

GH4099 is considered difficult to weld due to its high cracking susceptibility related to high Al + Ti contents. The intergranular cracks were found particularly at columnar grain boundaries align along the building direction in as-EBM condition PREPed sample shown in Figure 8c, no transverse cracks and lack of fusion phenomenon were observed, indicating that the crack is intergranular crack. Figure 13c,d show the secondary electron images of the crack surface from a broken open PREPed sample, which was cut into a 2 mm thickness sheet in the X-Z plane and pried it apart running along the crack lines. The observation of fracture surface shows the presence of discrete liquid films in quantities, which were wetting the dendrites when cracking occurred. It is clearly that the high cooling rate for EBM process leaves magnitude of residual stresses, further evaluates the susceptibility of solidification cracking in presence of liquid films. On the other hand, thermal stresses during the last stage of solidification pulling on the liquid films results in cracking [20]. EBM melting process is a quite complicated course with re-melting, partial re-melting, cyclic annealing, etc. [20]. It is hard to identify the existing crack propagated as solidification cracking or liquation cracking. For solidification cracking, dendrite formation inhibits the flow of the remaining liquid in the interdendritic regions, where act as crack initiation points under the effect of the stress induced by solidification. Liquation cracking is generally reported to occur in a position away from the melt pool where the material is heated rapidly to a temperature which is lower than the overall liquidus of the material [36, 37]. Whereas fracture surface of crack-free GAed sample exhibit dimple-like features as a response to a typical ductile failure shown in Figure 13b.

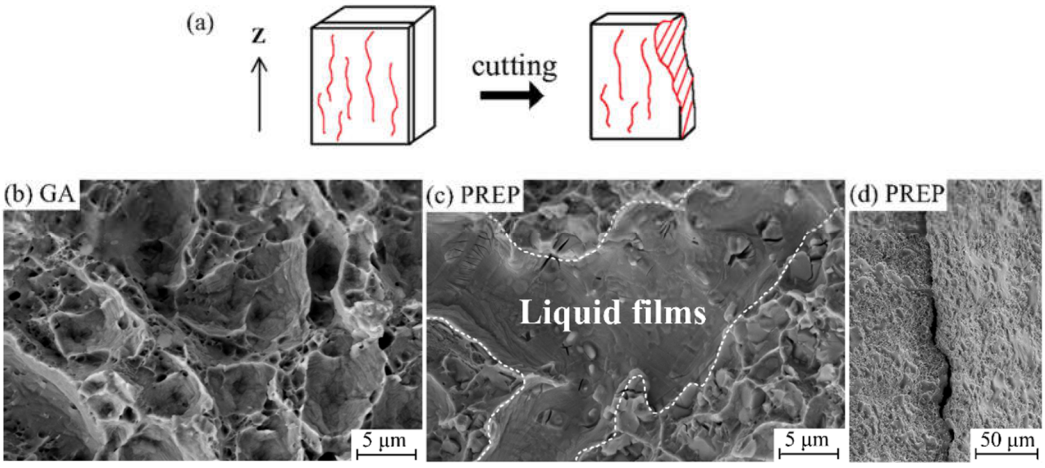

Figure 13. High magnification SE-SEM images of fracture surface from: (**b**) GAed sample, (**c**) a broken open PREPed sample, and (**d**) low magnification of (**c**). (**a**) Illustration of a broken open PREPed sample.

Li et al. [38] reported that the crack initiated with the assistance of the transverse tensile strain/stress tearing up the liquid film formed by the low-melting point pre-exist-

Preprints (www.preprints.org) | NOT PEER-REVIEWED | Posted: 12 July 2022 doi:10.20944/preprints202207.0169.v1

ing phases in the primary heat affected zone, such as γ/γ′ eutectics and coarse γ′ precipitates, Thermal contraction and re-precipitation of secondary γ′ leads to high density of dislocations at the γ/γ′ interface, further accelerates the separation of liquid film from grain boundary as well. Chauvet et al. [20] studied the fracture surface of a non-weldable nickel-based superalloy fabricated by powder bed-based selective electron beam melting (S-EBM), and the dendritic morphology with a limited development of secondary arms indicated the presence of intergranular liquid films in the upper part. As top layer has a limited shrinkage from former solidified layers, surface tensile effects turn out to be detrimental when tensile stress applied to liquid film wetting dendrites. They also found the cracks associated to the presence of liquid film propagate along high angle grain boundaries (misorientation > 15°) whereas low angle grain boundaries (misorientation < 15°) remain uncracked. Zhang et al. [39] established a mathematical model, which explained that different volume fraction of remaining liquid in CM247LC and IN792 Ni-based superalloys resulted in high strains and strain rates, thus affected crack formation and castability. The size of freezing range in the two-phase mushy zone contributes to the alloys property which but not only decided hot tearing resistance, Refs. [39, 40]. Moreover, hot tears occur when the solid dendrite arms do not coalesce and liquid still continuously present in between the dendrites above the coherency temperature, associated to deformation by tensile stresses applying to the non-coherent dendrite network with insufficient liquid [40]. As to a non-weldable nickel-based superalloy, Kontis et al. [4] found the amount of solutes segregation of namely B, Mo and Cr to HAGBs, leading to the occurrence of liquid films where concentration in the liquid reached the critical composition to form borides along with the solidification stresses. They also identified the hot cracking caused by grain boundary segregation, referred to as “segregation induced liquation”, over the course of remelting and deposition of the subsequent layers in additive manufacture process.

4.2. Effect of Si Segregation on Cracking Behaviours

EPMA analysis represents the element distribution on fracture surface of PREPed sample in the X-Z plane. As shown in Figure 14, it can be observed that there are distinct Si and O enrichment at the crack edge, indicating that enrichment of trace elements such as Si contributes to the crack formation.

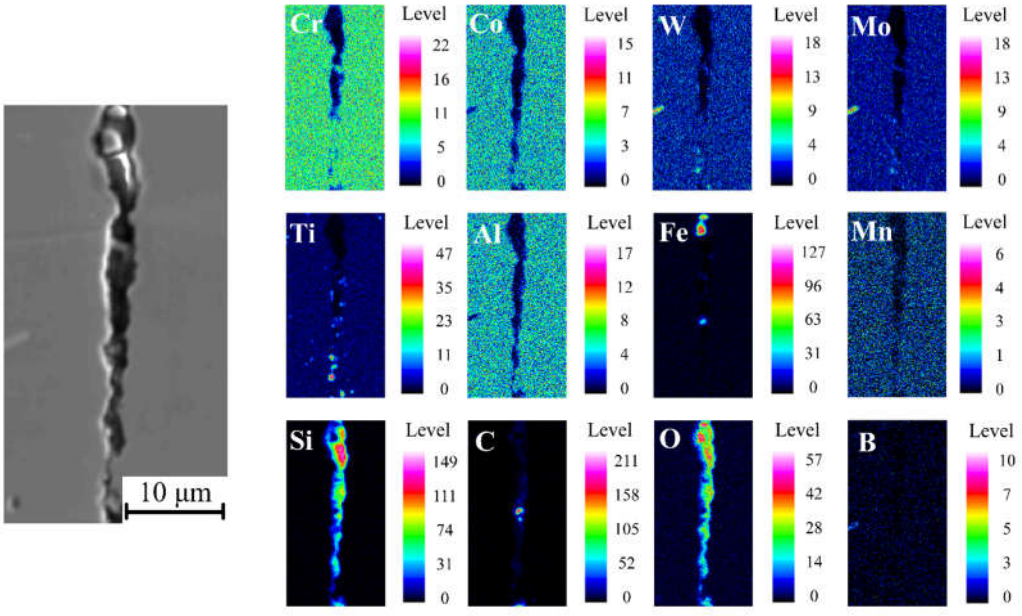

Figure 14. Series of elemental maps by EPMA showing the distribution nearby crack of key elements in as-EBM PREPed GH4099 superalloy. The coloured scale bar at the right shows relative concentration, showing Si and O enrichment. Map conditions: 0.2 μm step size both in x and y, 20kV.

Cloots et al. [41] revealed that cracks of IN738LC samples processed by selective laser melting propagate along building direction and distribute in a large grain boundary, crack surface seemed to be wetted with a liquid film were detected by atom probe tomography (APT), indicating the segregation of Zr at grain boundaries, which is a possible reason for hot cracking during SLM process because it dramatically lowers the solidus temperature of IN738LC. Zhao et al. [42] investigated fracture surface in René88DT superalloy prepared by laser solid forming (LSF) and formation of re-solidified products along grain boundaries in HAZ can be found, EDS analysis results represented that these re-solidified products within the cracks, containing high amount of Ti, Al, Cr, Co and Ni, are the re-solidified (γ+γ′) eutectics, speculated that HAZ cracking results from the liquation cracking. Engeli et al. [43] investigated crack density of IN738LC samples with different amount of Si content fabricated by selective laser melting and found that the fraction of Si has a strong detrimental effect to the crack density even on a small amount < 0.2 wt.% as well as its SLM processability.

It is well known from previous works that minor elements including C, B, S, P, Mg, etc. strongly influence the weldability of Ni-based superalloys even on ppm level [34]. Silicon may be used as refining addition and deoxidizer to improve weldability and oxidation resistance during traditional melting process, but its detrimental effect presented in the final alloys must be considered according to Ref. [44].

ICP-AES results of chemical composition of the GA and PREP GH4099 powders in Table 1 show that the Si content of the PREP powder is higher by one order of magnitude than that of the GA powder. It can be seen that GH4099 sample deposited with the PREP powder which mixed a larger content of Si from vendors, thereby increases the crack sensitivity during the EBM forming process, inducing the occurrence of intergranular crack.

5. Conclusions

GH4099 superalloy samples were successfully fabricated by EBM by using GA and PREP powders. Several observations and conclusions are drawn.

(1) Dense and crack-free samples were built at 980 ℃ for the GA powder. By contrast, cracks were observed in the PREP sample built at 1100 ℃. For both cases, fine spherical γ′ phase precipitated uniformly with a volume fraction of ~20%.
(2) Local enrichment of minor element Si was responsible for the cracking behaviour of the PREP sample.
(3) The cracks were successfully healed by HIPing and heat treatment.
(4) Tensile properties of the GA and PREP samples in the build direction are comparable to the wrought superalloy. However, the healed cracks remain weak in the horizontal direction.

Acknowledgments: This research was supported by the National Science and Technology Major Project (J2019-VII-0016-0157) and National Key Research and Development Program of China (2021YFB3700501).

Author Contributions: Shixing Wang conceived and designed the experiment, performed the experiments and wrote the paper; Shen Tao analyzed the data and discussed the results; Hui Peng designed the experiment and wrote the paper.

Conflicts of Interest: The authors declare no conflicts of interest.

References

1. Reed, R. C., *The superalloys : fundamentals and applications*. Cambridge University Press: Cambridge, UK ; New York, 2006; p xiv, 372 p.
2. Murray, S. P.; Pusch, K. M.; Polonsky, A. T.; Torbet, C. J.; Seward, G. G. E.; Zhou, N.; Forsik, S. A. J.; Nandwana, P.; Kirka, M. M.; Dehoff, R. R.; Slye, W. E.; Pollock, T. M., A defect-resistant Co-Ni superalloy for 3D printing. *Nature Communications* **2020,** *11* (1).
3. Sotov, A. V.; Agapovichev, A. V.; Smelov, V. G.; Kokareva, V. V.; Dmitrieva, M. O.; Melnikov, A. A.; Golanov, S. P.; Anurov, Y. M., Investigation of the IN-738 superalloy microstructure and mechanical properties for the manufacturing of gas turbine engine nozzle guide vane by selective laser melting. *International Journal of Advanced Manufacturing Technology* **2020,** *107* (5-6), 2525-2535.
4. Kontis, P.; Chauvet, E.; Peng, Z.; He, J.; da Silva, A. K.; Raabe, D.; Tassin, C.; Blandin, J.-J.; Abed, S.; Dendievel, R.; Gault, B.;

Martin, G., Atomic-scale grain boundary engineering to overcome hot-cracking in additively-manufactured superalloys. *Acta Materialia* **2019,** *177*, 209-221.
5. Yao, Y.; Xing, C.; Peng, H.; Guo, H.; Chen, B., Solidification microstructure and tensile deformation mechanisms of selective electron beam melted Ni3Al-based alloy at room and elevated temperatures. *Materials Science and Engineering a-Structural Materials Properties Microstructure and Processing* **2021,** *802*.
6. Peng, H.; Shi, Y.; Gong, S.; Guo, H.; Chen, B., Microstructure, mechanical properties and cracking behaviour in gamma '-precipitation strengthened nickel-base superalloy fabricated by electron beam melting. *Materials & Design* **2018,** *159*, 155-169.
7. Ramsperger, M.; Singer, R. F.; Korner, C., Microstructure of the Nickel-Base Superalloy CMSX-4 Fabricated by Selective Electron Beam Melting. *Metallurgical and Materials Transactions a-Physical Metallurgy and Materials Science* **2016,** *47A* (3), 1469-1480.
8. Chauvet, E.; Tassin, C.; Blandin, J.-J.; Dendievel, R.; Martin, G., Producing Ni-base superalloys single crystal by selective electron beam melting. *Scripta Materialia* **2018,** *152*, 15-19.
9. Fernandez-Zelaia, P.; Kirka, M. M.; Rossy, A. M.; Lee, Y.; Dryepondt, S. N., Nickel-based superalloy single crystals fabricated via electron beam melting. *Acta Materialia* **2021,** *216*.
10. Kuo, Y. L.; Kamigaichi, A.; Kakehi, K., Characterization of Ni-Based Superalloy Built by Selective Laser Melting and Electron Beam Melting. *Metallurgical and Materials Transactions a-Physical Metallurgy and Materials Science* **2018,** *49A* (9), 3831-3837.
11. Gaumann, M.; Henry, S.; Cleton, F.; Wagniere, J. D.; Kurz, W., Epitaxial laser metal forming: analysis of microstructure formation. *Materials Science and Engineering a-Structural Materials Properties Microstructure and Processing* **1999,** *271* (1-2), 232-241.
12. Acharya, R.; Bansal, R.; Gambone, J. J.; Das, S., A Coupled Thermal, Fluid Flow, and Solidification Model for the Processing of Single-Crystal Alloy CMSX-4 Through Scanning Laser Epitaxy for Turbine Engine Hot-Section Component Repair (Part I). *Metallurgical and Materials Transactions B-Process Metallurgy and Materials Processing Science* **2014,** *45* (6), 2247-2261.
13. Basak, A.; Acharya, R.; Das, S., Additive Manufacturing of Single-Crystal Superalloy CMSX-4 Through Scanning Laser Epitaxy: Computational Modeling, Experimental Process Development, and Process Parameter Optimization. *Metallurgical and Materials Transactions a-Physical Metallurgy and Materials Science* **2016,** *47A* (8), 3845-3859.
14. Basak, A.; Das, S., Additive Manufacturing of Nickel-Base Superalloy Rene N5 through Scanning Laser Epitaxy (SLE) - Material Processing, Microstructures, and Microhardness Properties. *Advanced Engineering Materials* **2017,** *19* (3).
15. Kirka, M. M.; Unocic, K. A.; Raghavan, N.; Medina, F.; Dehoff, R. R.; Babu, S. S., Microstructure Development in Electron Beam-Melted Inconel 718 and Associated Tensile Properties. *Jom* **2016,** *68* (3), 1012-1020.
16. Korner, C.; Ramsperger, M.; Meid, C.; Burger, D.; Wollgramm, P.; Bartsch, M.; Eggeler, G., Microstructure and Mechanical Properties of CMSX-4 Single Crystals Prepared by Additive Manufacturing. *Metallurgical and Materials Transactions a-Physical Metallurgy and Materials Science* **2018,** *49A* (9), 3781-3792.
17. DuPont, J. N.; Lippold, J. C.; Kiser, S. D., *Welding metallurgy and weldability of nickel-base alloys*. John Wiley & Sons: Hoboken, N.J., 2009; p xiv, 440 p.
18. Burger, D.; Parsa, A. B.; Ramsperger, M.; Korner, C.; Eggeler, G., Creep properties of single crystal Ni-base superalloys (SX): A comparison between conventionally cast and additive manufactured CMSX-4 materials. *Materials Science and Engineering a-Structural Materials Properties Microstructure and Processing* **2019,** *762*.
19. Wollgramm, P.; Burger, D.; Parsa, A. B.; Neuking, K.; Eggeler, G., The effect of stress, temperature and loading direction on the creep behaviour of Ni-base single crystal superalloy miniature tensile specimens. *Materials at High Temperatures* **2016,** *33* (4-5), 346-360.
20. Chauvet, E.; Kontis, P.; Jaegle, E. A.; Gault, B.; Raabe, D.; Tassin, C.; Blandin, J.-J.; Dendievel, R.; Vayre, B.; Abed, S.; Martin, G., Hot cracking mechanism affecting a non-weldable Ni-based superalloy produced by selective electron Beam Melting. *Acta Materialia* **2018,** *142*, 82-94.
21. Unocic, K. A.; Kirka, M. M.; Cakmak, E.; Greeley, D.; Okello, A. O.; Dryepondt, S., Evaluation of additive electron beam melting of haynes 282 alloy. *Materials Science and Engineering a-Structural Materials Properties Microstructure and Processing* **2020,** *772*.
22. Zhong, C. L.; Chen, J.; Linnenbrink, S.; Gasser, A.; Sui, S.; Poprawe, R., A comparative study of Inconel 718 formed by High Deposition Rate Laser Metal Deposition with GA powder and PREP powder. *Materials & Design* **2016,** *107*, 386-392.
23. Ding, P. P.; Mao, A. Q.; Zhang, X.; Jin, X.; Wang, B.; Liu, M.; Gu, X. L., Preparation, characterization and properties of multicomponent A1CoCrFeNi(2.1) powder by gas atomization method. *Journal of Alloys and Compounds* **2017,** *721*, 609-614.
24. Chen, Y.; Zhang, J. Y.; Wang, B.; Yao, C. G., Comparative study of IN600 superalloy produced by two powder metallurgy technologies: Argon Atomizing and Plasma Rotating Electrode Process. *Vacuum* **2018,** *156*, 302-309.
25. Pleass, C.; Jothi, S., Influence of powder characteristics and additive manufacturing process parameters on the microstructure and mechanical behaviour of Inconel 625 fabricated by Selective Laser Melting. *Additive Manufacturing* **2018,** *24*, 419-431.
26. Nguyen, Q. B.; Nai, M. L. S.; Zhu, Z. G.; Sun, C. N.; Wei, J.; Zhou, W., Characteristics of Inconel Powders for Powder-Bed Additive Manufacturing. *Engineering* **2017,** *3* (5), 695-700.
27. Herzog, D.; Seyda, V.; Wycisk, E.; Emmelmann, C., Additive manufacturing of metals. *Acta Materialia* **2016,** *117*, 371-392.
28. Helmer, H. E.; Korner, C.; Singer, R. F., Additive manufacturing of nickel-based superalloy Inconel 718 by selective electron beam melting: Processing window and microstructure. *Journal of Materials Research* **2014,** *29* (17), 1987-1996.
29. Lopez-Galilea, I.; Ruttert, B.; He, J. Y.; Hammerschmidt, T.; Drautz, R.; Gault, B.; Theisen, W., Additive manufacturing of CMSX-4 Ni-base superalloy by selective laser melting: Influence of processing parameters and heat treatment. *Additive Manufacturing* **2019,** *30*.

30. Kirka, M. M.; Medina, F.; Dehoff, R.; Okello, A., Mechanical behavior of post-processed Inconel 718 manufactured through the electron beam melting process. *Materials Science and Engineering a-Structural Materials Properties Microstructure and Processing* **2017,** *680*, 338-346.
31. Harrison, N. J.; Todd, I.; Mumtaz, K., Reduction of micro-cracking in nickel superalloys processed by Selective Laser Melting: A fundamental alloy design approach. *Acta Materialia* **2015,** *94*, 59-68.
32. Cha, P. R.; Yeon, D. H.; Chung, S. H., Phase-field study for the splitting mechanism of coherent misfitting precipitates in anisotropic elastic media. *Scripta Materialia* **2005,** *52* (12), 1241-1245.
33. Yoo, Y. S., Morphological instability of spherical gamma ' precipitates in a nickel base superalloy. *Scripta Materialia* **2005,** *53* (1), 81-85.
34. Richards, N. L.; Chaturvedi, M. C., Effect of minor elements on weldability of nickel base superalloys. *International Materials Reviews* **2000,** *45* (3), 109-129.
35. Balachandramurthi, A. R.; Moverare, J.; Mahade, S.; Pederson, R., Additive Manufacturing of Alloy 718 via Electron Beam Melting: Effect of Post-Treatment on the Microstructure and the Mechanical Properties. *Materials* **2019,** *12* (1).
36. Dye, D.; Hunziker, O.; Reed, R. C., Numerical analysis of the weldability of superalloys. *Acta Materialia* **2001,** *49* (4), 683-697.
37. Carter, L. N.; Attallah, M. M.; Reed, R. C. In *Laser Powder Bed Fabrication of Nickel-Base Superalloys: Influence of Parameters; Characterisation, Quantification and Mitigation of Cracking*, 12th International Symposium on Superalloys, Seven Springs, PA, Sep 09-13; Seven Springs, PA, 2012; pp 577-586.
38. Li, Y.; Chen, K.; Tamura, N., Mechanism of heat affected zone cracking in Ni-based superalloy DZ125L fabricated by laser 3D printing technique. *Materials & Design* **2018,** *150*, 171-181.
39. Zhang, J.; Singer, R. F., Hot tearing of nickel-based superalloys during directional solidification. *Acta Materialia* **2002,** *50* (7), 1869-1879.
40. Rappaz, M.; Drezet, J.; Gremaud, M., A New Hot-Tearing Criterion. *Metallurgical and Materials Transactions a-Physical Metallurgy and Materials Science* **1999,** *30*, 449–455.
41. Cloots, M.; Uggowitzer, P. J.; Wegener, K., Investigations on the microstructure and crack formation of IN738LC samples processed by selective laser melting using Gaussian and doughnut profiles. *Materials & Design* **2016,** *89*, 770-784.
42. Zhao, X. M.; Lin, X.; Chen, J.; Xue, L.; Huang, W. D., The effect of hot isostatic pressing on crack healing, microstructure, mechanical properties of Rene88DT superalloy prepared by laser solid forming. *Materials Science and Engineering a-Structural Materials Properties Microstructure and Processing* **2009,** *504* (1-2), 129-134.
43. Engeli, R.; Etter, T.; Geiger, F.; Stankowski, A.; Wegener, K., Effect of Si on the SLM processability of IN738LC. In *International Solid Freeform Fabrication Symposium*, Austin, America, 2015; pp 823-831.
44. Holt, R. T.; Wallace, W., Impurities and Trace Elements in Nickel-Base Superalloys. *International Metals Reviews* **1976,** *21* (1), 1-24.